Science and Technology for Energy Transition **79**, 78 (2024)

https://doi.org/10.2516/stet/2024080

STET
Available online at:
stet-review.org

**Decarbonizing Energy Systems: Smart Grid and Renewable Technologies**
Fang Rui-ming and Qiangqiang Liao (Guest Editors)

REGULAR ARTICLE OPEN ACCESS

# Synergistic enhancement of photoelectrocatalytic activity and photostability in CdS photoanodes by ultrathin polydopamine layer

Zhiru Zhao[1,2], Mingyue Wang[2], Shuya Zheng[2], Quanqing Zhang[1], Lu Han[2,*], and Xibao Li[3,*]

[1] School of Materials Science and Engineering, Yingkou Institute of Technology, Yingkou 115000, PR China
[2] School of Materials and Metallurgy, University of Science and Technology Liaoning, Anshan 114051, PR China
[3] School of Materials Science and Engineering, Nanchang Hangkong University, Nanchang 330063, PR China

Received: 29 June 2024 / Accepted: 3 September 2024

**Abstract.** CdS-based photocatalyst and photoanode have recently drawn the attention of several investigators primarily in connection with its excellent visible light response in various catalytic reactions involving light, especially photoelectrochemical (PEC) water splitting. The present approach highlights the concept of constructing a biological functional layer incorporated for photochemical instable semiconductors for practical PEC applications. However, practical applications of CdS-based photoanodes are limited by rapid charge recombination and severe photo corrosion. This study introduces a novel approach to enhance reaction kinetics and stability. We present a CdS nanorod photoanode with an ultrathin layer of polydopamine (PDA), prepared through a conformal polymerization assembly process, which serves as a robust platform for subsequent assembly of hole cocatalysts FeOOH. The resulting sandwich structure of CdS/PDA/FeOOH photoanode demonstrates an incident to current efficiency (IPCE) of 7.1% at 420 nm and a photocurrent of 1.9 mA/cm$^2$ at 1.23 V versus the reversible hydrogen potential (RHE). The integrated photoanode exhibits significantly prolonged photostability compared to CdS, CdS/PDA, and CdS/FeOOH photoanodes. The significance of this work lies in constructing a FeOOH structure (with hole extraction and consumption capabilities) on the CdS outermost layer using an easy-to-operate preparation process, thereby revealing the ability of PDA to enable the passage of photogenerated holes. The present approach highlights the concept of integrating biologically functional layers to stabilize photochemically unstable semiconductors for practical PEC applications.

**Keywords:** Polydopamine, Hole transport, CdS photoanode, Photocorrosion, Charge separation.

## 1 Introduction

In response to escalating environmental pollution and energy crises, photoelectric energy conversion has emerged as a promising solution. This method harnesses the benefits of controllable electron-driven electrocatalysis and energy-saving photocatalysis [1–3]. However, the sluggish oxygen evolution reaction (OER) occurring at the photoanode hampers the efficiency of photoelectrochemical (PEC) water splitting [4]. Several semiconductors have been developed for use as photoanodes, including $TiO_2$ [5, 6], $WO_3$ [7, 8], $BiVO_4$ [9], and CdS [10–12]. Among these, CdS is considered particularly promising due to its suitable bandgap (2.2–2.4 eV) and appropriate band-edge placements. The rapid recombination of photoexcited charge carriers notably diminishes the effectiveness of OER [13]. Furthermore, the self-decomposition of CdS compromises its stability during use [14].

Owing to the improved charge separation derived by a built-in electric field, recent research advances have attached importance to the construction of various heterojunctions, such as type II, Z-Scheme, and S-Scheme band alignment [15–18]. Therefore, the combination of CdS with another semiconductor enhances the transfer of photoexcited charges, thereby improving the kinetics of the OER reaction to a certain degree. More recently, additional attempts have been made to speed up hole transfer by incorporating amorphous hole cocatalysts, such as FeOOH [19], CoOOH [20], and NiOOH [21], onto heterojunction photoanodes. Combining hydroxy oxides with CdS achieves a dual purpose. On one hand, it enhances the transfer rate

* Corresponding authors: hanlu@ustl.edu.cn (Lu Han); lixibao@nchu.edu.cn (Xibao Li)

of photogenerated holes of CdS, which aids in accelerating the kinetics of the OER. On the other hand, it increases the photostability of CdS, as the transformation of sulfur ions into elemental sulfur occurs as a result of oxidation by photogenerated holes.

Passivating over-layer is frequently suggested as a means to augment reaction kinetics and reinforce stability when dealing with semiconductors prone to photochemical degradation. Ultrathin layers such as $TiO_2$ [22], $Al_2O_3$ [23], and polyaniline (PANI) [24] have garnered widespread recognition due to their effectiveness in mitigating surface charge recombination and shielding photoelectrodes against chemical deterioration in the surrounding electrolyte atmosphere. Polydopamine (PDA), as a nature-inspired polymer, is valued for biomedical applications [25]. In recent years, considerable interest has been attracted in photoelectric energy conversion applications due to some gradually recognized features such as sensibilization, hydrophilicity, adhesive capability, and biocompatibility [26–28]. Nevertheless, the capabilities of PDA within the realm of photoelectrocatalysis remain underutilized, with its precise operational processes yet to be comprehensively delineated.

Prior research endeavors have been undertaken by us, focusing on the functional aspects associated with PDA for PEC hydrogen evolution. A recently developed hierarchical heterostructure of CdS@PDA/$TiO_2$ has revealed improved PEC stability due to the protective layer of PDA, which guards against the photo corrosion of CdS. The superior PEC performance is credited to the photosensitization effects and the boosted carrier transport facilitated by the PDA component [29]. We subsequently disclosed a trinary composite photocathode composed of $Cu_2O$, PDA, and $TiO_2$. The incorporation of PDA enhances the interfacial bonding within the $TiO_2/Cu_2O$ heterojunction, providing a steady driving force for the segregation of charges [30, 31]. The body of work to date has established the PDA layer's proficiency in facilitating the transport of photogenerated electrons. Yet, in light of the susceptibility of CdS to photo corrosion caused by photoinduced holes, it becomes imperative to determine if the PDA layer can similarly accommodate the movement of these holes. This line of inquiry is of substantial importance as it unveils opportunities to delve into additional properties of PDA, thereby enriching the scope for future research.

Herein, we have meticulously crafted a prospective PDA thin coating on a CdS photoelectrode. Recognizing the significance of the PDA's passivating impact and the pivotal role of hole cocatalysts, we then strategically adorned the PDA surface with FeOOH nanoparticles through an accessible hydrolysis method. The resulting assembly, a robust CdS/PDA/FeOOH photoanode, exhibited enhanced performance and durability under photoelectrochemical conditions. This suffices to demonstrate that the PDA layer permits the passage of photogenerated holes. This advancement heralds a wave of optimism for the photoelectrochemical conversion field, with multifunctional PDA at its core, promising a new direction for energy conversion technologies.

## 2 Experimental

### 2.1 Materials

Tetrahydrate of cadmium nitrate ($Cd(NO_3)_2{\cdot}4H_2O$), thiourea ($CH_4N_2S$), glutathione, tris-hydrochloride buffer (PH = 8.8), dopamine hydrochloride, iron chloride hexahydrate ($FeCl_3{\cdot}7H_2O$), hydrochloric acid (0.01 M), acetone, absolute ethanol, deionized water, sodium sulfate anhydrous ($Na_2SO_4$), glass made of tin oxide (FTO) doped with fluorine (14 **Ω**, 20 * 20 * 16 mm).

### 2.2 Preparation of photoelectrodes

CdS nanorod arrays were synthesized on FTO substrates utilizing a hydrothermal technique [10]. First, FTO substrates were sonicated for 30 min each in acetone, pure ethanol, and deionized water. Then, 0.0926 g of $Cd(NO_3)_2{\cdot}4H_2O$, 0.0228 g of $CH_4N_2S$, 0.0553 g of glutathione, and well combined in 10 mL of deionized water in a 25 mL reactor. Afterward, the dried FTO conductive surface was tilted downward and placed in the reactor solution, which was then heated at 200 °C for 8 h. The samples were chilled at the end, washed with deionized water, and then vacuum dried at 60 °C for 6 h, resulting in the deposition of CdS nanorod arrays on the FTO substrate.

Dopamine self-polymerization was employed to fabricate CdS/PDA electrodes as described in prior studies [29, 30]. Initially, dopamine hydrochloride weighing 0.1 g was dissolved in a combined solution consisting of 20 mL of tris-hydrochloride buffer and 30 mL of pure deionized water to achieve a final dopamine concentration of 2.0 g $L^{-1}$. The CdS photoelectrode was then submerged in this dopamine mixture and subjected to magnetic stirring for 10 min. Following this treatment, the photoelectrode surface was thoroughly rinsed with deionized water. To complete the process, the electrode was left to dry overnight at a temperature of 45 °C in an environment devoid of moisture within a vacuum oven.

FeOOH nanoparticles were synthesized and deposited onto a PDA-coated layer utilizing a straightforward hydrolysis method. To commence the process, 0.9461 g of $FeCl_3{\cdot}7H_2O$ was dissolved into a mixture that contained 50 mL of deionized water and 25 mL of 0.01 M hydrochloric acid solution. This solution was warmed to 60 °C using a controlled water bath and was subjected to continuous magnetic stirring for 12 h. Subsequently, the pristine CdS photoelectrode and the CdS electrode modified with a PDA layer were each dipped briefly into the iron solution, for a rapid 2-s interval, to achieve the formation of CdS/FeOOH and CdS/PDA/FeOOH composite photoelectrodes, respectively.

### 2.3 Characterization

High-resolution transmission electron microscopy (HR-TEM) and transmission electron microscopy (TEM) were utilized to assess the morphology of the as-prepared samples (FEI TalosF200x). Using an annular darkfield detector under TEM, the elemental mapping of energy-dispersive

X-ray spectroscopy (EDS) was studied. The crystal structure of the prepared samples was determined using an X-ray diffractometer using Cu Ka radiation (X' Pert Powder, PANalytical B.V.). The Thermo Scientific Nicolet iS5 Fourier transform infrared (FTIR) spectrometer was utilized to capture the 400–4000 $cm^{-1}$ FTIR spectra. The chemical state and elemental compositions were recorded using an X-ray photoelectron spectroscopy (XPS, Thermo Scientific K-Alpha, UK).

### 2.4 Photoelectrochemical tests

The photoelectrochemical (PEC) properties of the prepared samples were evaluated using a CHI760E electrochemical workstation (Chenhua, Shanghai) configured with a three-electrode system. The testing employed a 0.25 M $Na_2SO_4$ solution as the electrolyte. A standard Ag/AgCl electrode, platinum sheets, and the fabricated samples served as the reference, counter, and working electrodes, respectively. A 300 W xenon lamp (MICROSOLAR300, by Beijing Perfectlight Technology Co., Ltd., China) was used as the illumination source.

The current-voltage (J-V) profiles were recorded under alternating light and dark conditions. Each sample underwent linear sweep voltammetry (LSV) at a scan rate of 5 mV $s^{-1}$, across a potential window from −1 to 1 V versus RHE. To ascertain the incident photoelectric conversion efficiency (IPCE), the samples' ability to convert light into electrical current is assessed over a range of wavelengths from 350 to 700 nm by employing different filters. To calculate the efficiency of converting light into electrical current under an applied bias, the applied bias photon-to-current efficiency (ABPE) is assessed. Elevated values of ABPE suggest a more effective photoelectrochemical process for harnessing solar energy as electrical power. Potential sweeps were conducted in Mott-Schottky measurements between 0.5 and 0.7 V vs. Ag/AgCl. The study employed electrochemical impedance spectroscopy (EIS) with an AC amplitude of 5 mV and a frequency range of 100 kHz to 1 Hz. Under lighting conditions, at an open circuit voltage, the measured EIS values were obtained.

## 3 Results and discussion

Figure 1(a) illustrates the procedural schematic for crafting the hybrid CdS/PDA/FeOOH structure. In Figure 1(b), we observe the formation of CdS nanorods characterized by an average edge dimension close to 100 nm. These rods are noted to be enveloped by a distinct layer, dotted with particulate matter. The HRTEM images in Figure 1(c) and 1(d) reveal pristine lattice fringes with spacings of 0.336 and 0.315 nm, aligning with the (002) and (101) crystalline facets of CdS, as referenced in [32]. Additionally, fringe measurements of 0.23 nm and 0.16 nm are identified with the outer surface's composition, corresponding to the (200) and (022) planes of FeOOH [33]. Positioned between these layers, we postulate the existence of a PDA interlayer. Further validation of the multilayered configuration of CdS/PDA/FeOOH is provided through the HAADF-STEM imagery in Figure 1(e) and 1(f), showcasing the even spread of both PDA and FeOOH upon the CdS framework, hinting at a consistent, sandwich-like architecture. Complementing these observations, spatially resolved EDS mapping in Figure 1(g) corroborates the integration of CdS nanorods within a PDA shell, interspersed with FeOOH at the nanoscale, with an even distribution of the elemental constituents Cd, S, N, Fe, and O throughout the composite material.

The CdS/PDA/FeOOH composite sample's diffraction of X-rays (XRD) patterns appear in Figure 2(a). The hexagonal phase CdS is shown by a recognizable XRD pattern at 26.5° of the (002) crystal plane (JCPDS No. 01-075-1545) [32]. The peak at 37.31° is attributed to $SnO_2$ present in the FTO substrate. The peaks at 34.52° and 65.11° are characteristic peaks of FeOOH, and their diffraction peaks match the standard cards (JCPDS No. 01-077-0452) and (JCPDS No. 01-81-0462), respectively [33]. The XRD analysis confirms the incorporation of CdS and FeOOH within the photoelectrode's structure. Since PDA is an amorphous polymer, it does not produce a discernible pattern in the XRD analysis. Figure 2(b) presents the FTIR spectroscopy data for the series of samples prepared. The spectrum exhibits a characteristic absorption band at 627 $cm^{-1}$, which is attributed to the bending vibrations of N-H bonds. Peaks observed within the 775 $cm^{-1}$ region and a broad range from 2800 to 3000 $cm^{-1}$ correspond to the bending vibrations of C-H bonds and stretching vibrations, respectively, suggesting that there are benzene ring structures within the samples, as noted in reference [34]. In addition, peaks between 1270 and 1620 $cm^{-1}$ were considered to be the characteristic peaks of -$NH_2$, further confirming the presence of PDA [35]. Within FeOOH, the peak at 775 $cm^{-1}$ is attributed to the Fe-O stretching vibrations, in which the characteristic peak is attributed to the stretching and bending vibrations of Fe-O and Fe-OH [36]. These FTIR patterns provide further evidence for the successful preparation of CdS/PDA/FeOOH composite.

An XPS study was performed to validate the surface chemical state information of the CdS/PDA/FeOOH composite. As shown in Figure 2(c), the two peaks of Cd $3d_{3/2}$ and Cd $3d_{5/2}$ occur at 411.1 and 404.4 eV, respectively, which correspond to the $Cd^{2+}$ of CdS. In Figure 2(d), the S $2p_{1/2}$ presents a peak at 162.2 eV and the S $2p_{3/2}$ at 161.0 eV, ascribed to $S^{2-}$ of CdS [29]. Figure 2(e) shows the peaks of Fe $2p_{3/2}$ (709.8 eV) and Fe $2p_{1/2}$ (723.5), attributed to $Fe^{3+}$ of FeOOH [20]. Meanwhile, the O 1 s signature is identifiable in Figure 2(f). Delving into the details shown in Figure 2(g), the presence of a peak at 400.5 eV in the narrow-scan XPS spectrum is noticeable, which is indicative of the amino (-$NH_2$) groups situated at the end of the PDA chain [29, 30]. The aforementioned peaks correspond nicely with the EDS element mapping in Figure 1(f). These XPS patterns are consistent with the previous results derived from the XRD spectra, strongly confirming the coupling of CdS, PDA, and FeOOH.

The transient photocurrent response to solar light irradiation is examined by examining the I-t curves for amperometry, as shown in Figure 3(a). The resulting

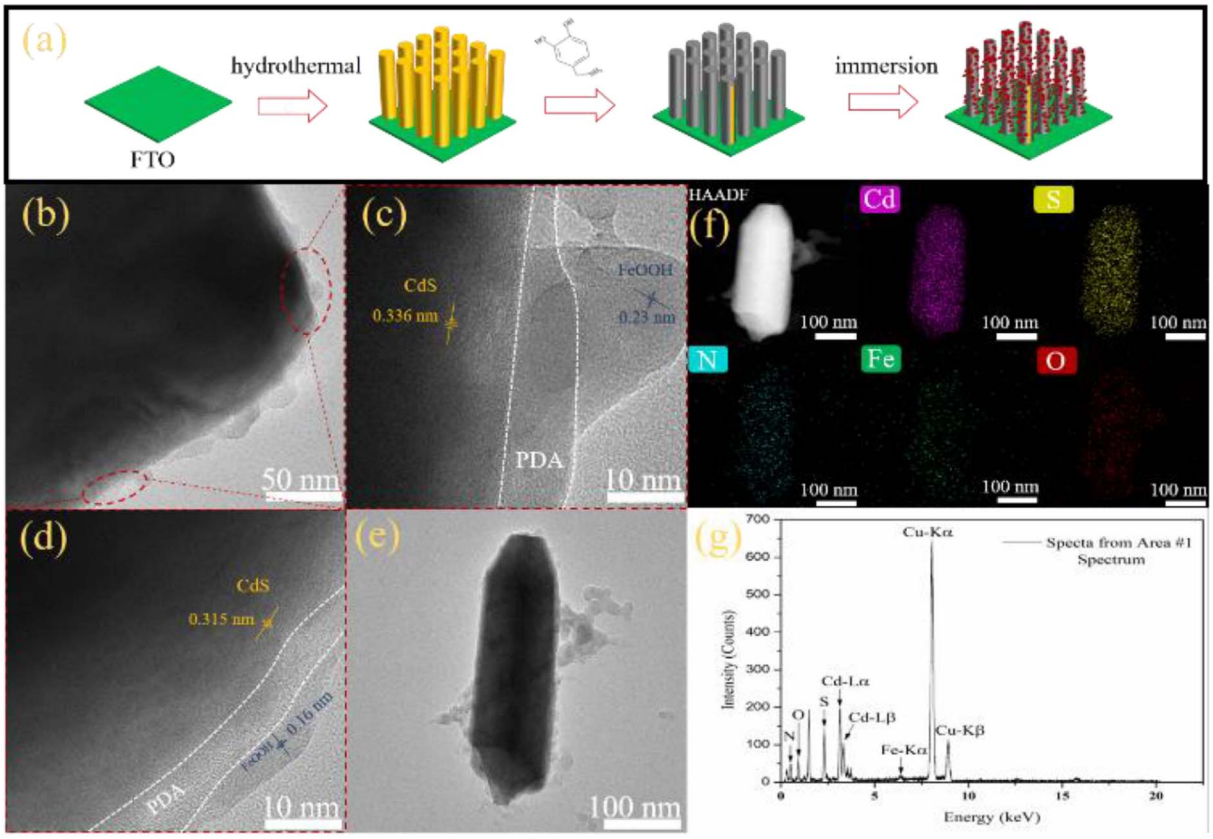


**Figure 1.** (a) An illustration of the procedures followed in the preparation of the CdS/PDA/FeOOH composite; (b) TEM image of CdS/PDA/FeOOH; (c, d) HRTEM of the area of choice indicated in (b); (e) TEM image of CdS/PDA/FeOOH; (f) EDS mapping for the CdS/PDA/FeOOH composite in (e); (g) Spectra from area in (f).

photoelectrodes exhibit a quick and renewable photocurrent response upon light switching. Bare CdS photoelectrode showed the lowest photocurrent density, attributed to the photogenerated carrier recombination caused by its surface defect state. The downward trend of photocurrent density is caused by its photo corrosion [10, 29]. For composite photoanodes with applied bias, relatively constant pattern photocurrent densities are recorded. On one hand, the ultrathin PDA overlayer improves CdS' absorption of visible light and particularly offers the best possible structural protection to ensure that active radicals dissolved in the electrolyte do not cause CdS photo corrosion. Moreover, given that FeOOH is acknowledged for its capability to extract holes [20], the strategic integration of FeOOH facilitates the movement of photogenerated holes, which primarily drives the photo corrosion of CdS. Coupling of PDA and FeOOH on CdS photoelectrode, CdS/PDA/FeOOH represents the remarkably enhanced photocurrent density and a positive impact on the stability in use. Specifically, it is important to note that the ultrathin PDA layer lacks light shielding; interestingly, it permits photogenerated hole passage. It is believed that this inference will be valuable for PDA in various photocatalytic reactions involving holes, after discovering that PDA has an electronic tunneling effect.

LSV curves depicted in Figure 3(b) illustrate the dependency of the photocurrent response on the voltage applied. Pristine CdS photoanode exhibits a high initial potential, indicating inferior photoactivity to other composite photoanodes. It is mainly caused by the slow OER dynamics on the surface of CdS. However, CdS/PDA, CdS/FeOOH and CdS/PDA/FeOOH composite photoanodes show a negative initial potential shift, indicating that OER occurs at a lower bias voltage. This shift is explained by the modification of the energy band structure brought about by the formation of heterojunctions. Pristine CdS has a photoresponse of 0.56 mA $cm^{-2}$ at 1.23 V vs. RHE due to the presence of surface recombination sites in practical applications; besides, CdS/PDA, CdS/FeOOH and CdS/PDA/FeOOH photoanodes are 0.9 mA $cm^{-2}$, 0.96 mA $cm^{-2}$ and 1.9 mA $cm^{-2}$, respectively. The notable enhancement in photocurrent density showcases the PDA layer's contribution to both photo-sensitivity enhancement and surface passivation [10, 29, 30]. Moreover, this layer aids in improving the separation and movement of charge carriers when the hole-extracting agent FeOOH is included. These interpretations are corroborated by data from HRTEM, XPS, IR, and I-t measurements. Further, the photocurrent density generated by CdS, CdS/FeOOH, and CdS/PDA/FeOOH is increased in a gradient manner.

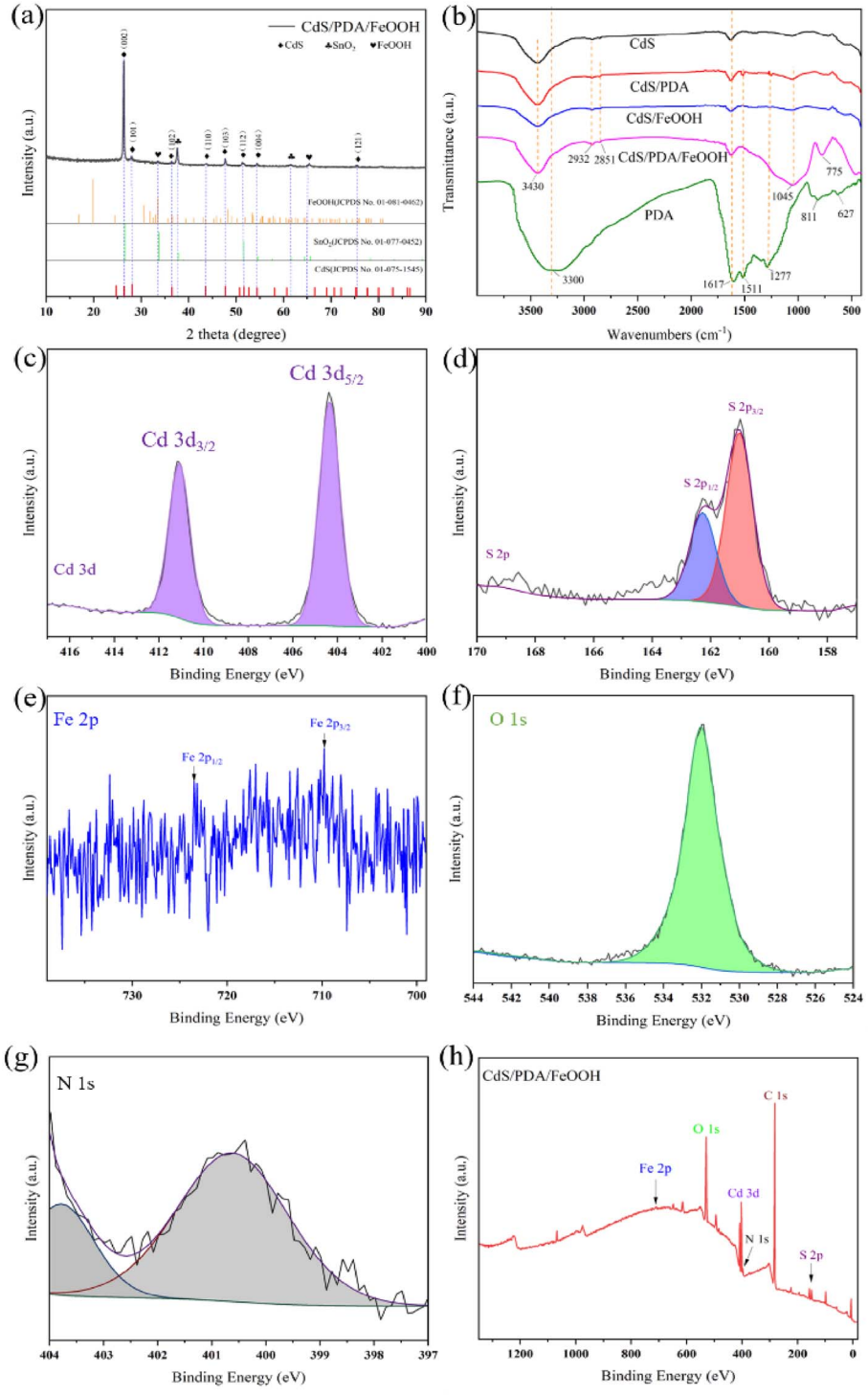


**Figure 2.** (a) XRD patterns of CdS/PDA/FeOOH; (b) FTIR spectra of CdS, CdS/PDA, CdS/FeOOH, CdS/PDA/FeOOH, PDA; (c–g) XPS fine spectra of Cd, S, Fe, O and N; (h) XPS full spectrum of CdS/PDA/FeOOH.

The result indicates that, as an intermediate layer, the PDA does not hinder the hole transmission, however, with the help of FeOOH, it makes it easier to separate electrons and holes. This transport mechanism significantly improves the visible light conversion efficiency of the composite photoanode. Figure 3(c) illustrates the applied bias to ABPE of the CdS/PDA/FeOOH composite photoanode, it reaches a maximum efficiency of 1% in energy conversion, surpassing the 0.46% and 0.48% of the CdS/FeOOH and CdS/PDA photoanodes, respectively. The lowest conversion rate can be observed in the pristine CdS photoanode, with a value of 0.29%.

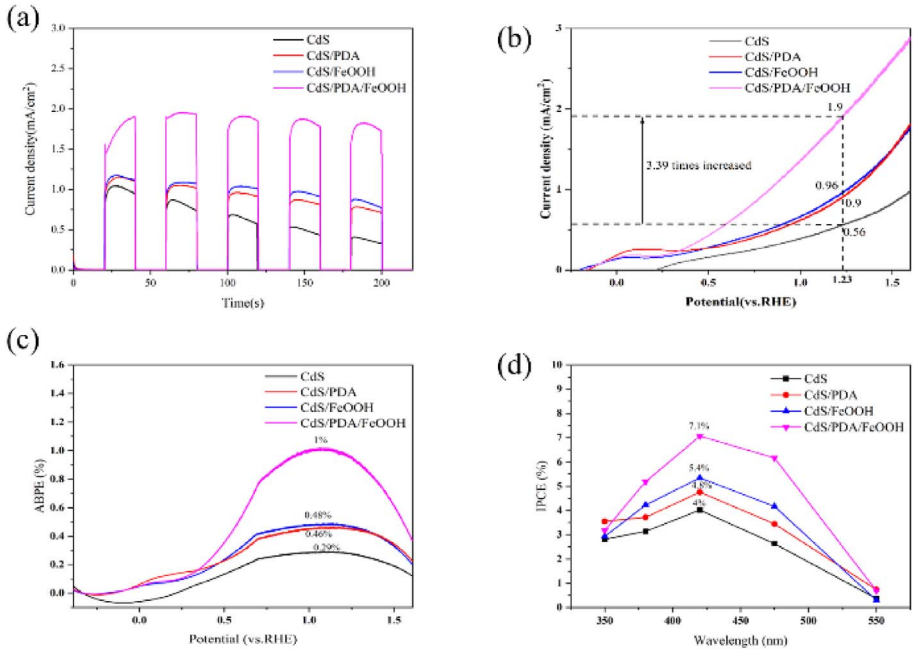


**Figure 3.** PEC performance of pure CdS, CdS/PDA, CdS/FeOOH, and CdS/PDA/FeOOH photoelectrodes. (a) I-t; (b) LSV; (c) ABPE; (d) IPCE.

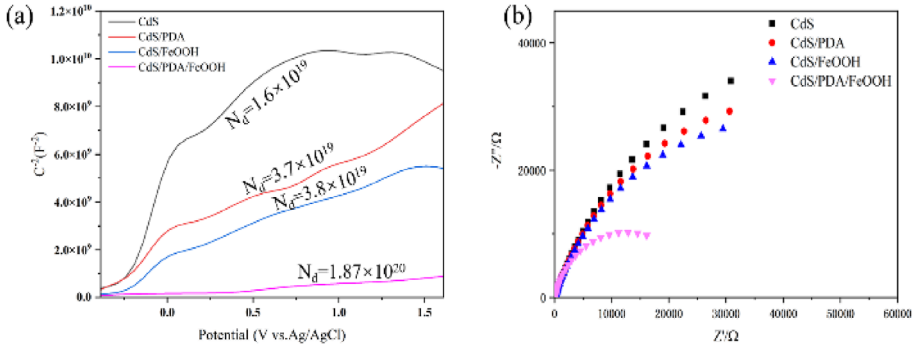


**Figure 4.** (a) M-S graphs recorded at a fixed frequency of 1 kHz; (b) EIS spectra under open circuit voltage.

To investigate the use of photons more thoroughly, the IPCE is tested in the wavelength range of 300–600 nm, as shown in Figure 3(d). At the monochromatic light with a wavelength of 420 nm, the maximum IPCE values are 4%, 4.8%, 5.4%, and 7.1% for CdS, CdS/PDA, CdS/FeOOH, and CdS/PDA/FeOOH photoanodes, respectively. The increased IPCE value of the composite photoanode indicates that more photogenerated electron-hole pairs are generated, allowing for sufficient electron and hole transport for subsequent water decomposition reaction at the electrode, thus prolonging the life of the photoanode. This once again confirms the ability of PDA to allow the passage of photogenerated holes.

A Mott-Schottky (M-S) analysis was performed on the electrodes to substantiate the enhancement in the transfer of holes through the PDA layer, facilitated by the addition of the FeOOH extractor. From the M-S diagram in Figure 4(a), the curves of the four photoanodes have positive slopes, demonstrating that they are all n-type semiconductors. The carrier concentrations of the CdS, CdS/PDA, CdS/FeOOH, and CdS/PDA/FeOOH photoanodes are calculated to be $1.6 \times 10^{19}$, $3.7 \times 10^{19}$, $3.8 \times 10^{19}$, and $1.87 \times 10^{20}$ $cm^{-3}$ respectively. Echoing the results of PEC performance in Figure 3, the carrier concentrations of the composite photoanodes are considerably greater than that of the CdS photoanode, and the CdS/PDA/FeOOH composite photoanode exhibits the highest concentration. As a result, this kinetically promotes carrier separation and transfer, which in turn increases the photocurrent density. Furthermore, an EIS examination was executed on the as-prepared CdS photoelectrodes. The corresponding EIS Nyquist diagrams for each photoelectrode are depicted in Figure 4(b). The significantly lower circle radius of the new photoelectrodes, as seen in the image, forecasts greater interfacial charge transfer capability and decreased interfacial charge transfer resistance. Therein,

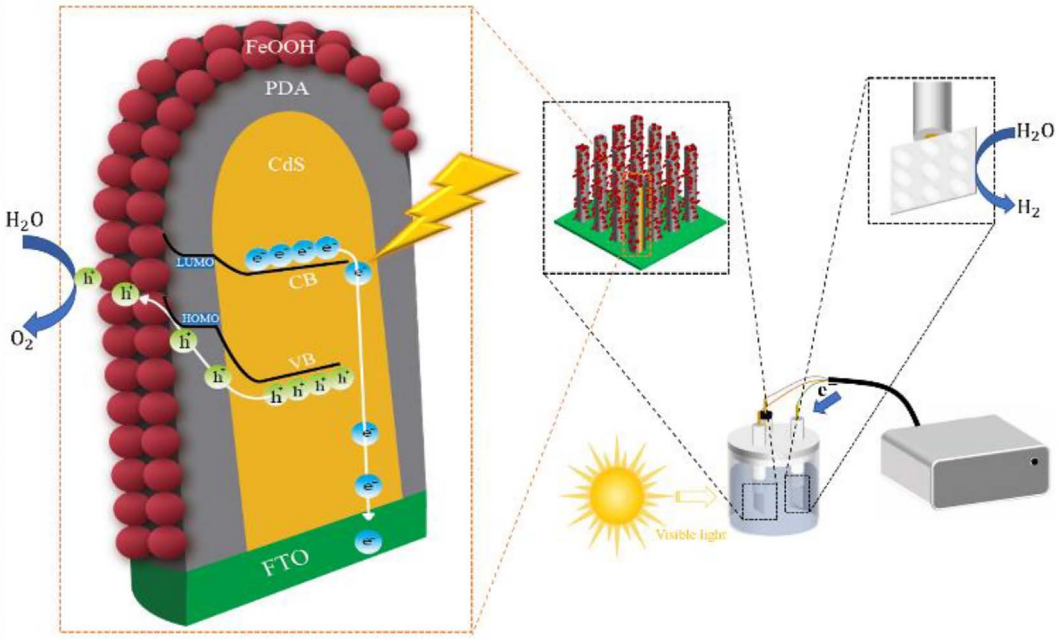


**Figure 5.** Mechanism of CdS/PDA/FeOOH photoelectrode for PEC water splitting.

**Table 1.** The functions of PDA in the field of PEC.

| Materials | Functions | Refs. |
|---|---|---|
| CdS/PDA/FeOOH | Passage of photogenerated holes | This work |
| CdS/PDA/Nafion | Reduces surface defects of CdS and facilitates Nafion coating | [10] |
| $TiO_2$/CdS@PDA | Co-photosensitization, and as a shelter against photo corrosion | [29] |
| $Cu_2O$/PDA/$TiO_2$ | Adhesive properties, hydrophilicity and passivation layer | [30] |
| CdS/PDA/Co-Pi | Enhance electron conductivity and form a passivation layer | [32] |
| g-$C_3N_4$@PDA/BiOBr | PDA as an efficient electron transfer mediator | [37] |
| $TiO_2$/PDA | Enhancing the hole–electron separation and harvesting visible light | [38] |
| Ti/$TiO_2$NT@PDA-AgNP | In situ reducing agent capable of reducing some metal ions | [39] |
| PDA15/ZnO/$Co_3O_4$ | Enhanced $CO_2$ adsorption/activation capacity by PDA modification | [40] |
| Ag/AgCl/PDA-$TiO_2$ | A stabilizer and reductant in fabricating the photocatalyst | [41] |

the CdS/PDA/FeOOH composite photoanode has the least impedance to charge transfer across surfaces and the smallest semicircle. This again demonstrates the synergistic effect of passivation and improved hole transferring on a higher carrier separation efficiency.

Potential processes of the ternary CdS/PDA/FeOOH composite photoanode for PEC increase in activity and stability have been further demonstrated in Figure 5 based on the analysis above. Under illumination, the OER on the pristine CdS electrode suffers from sluggish kinetics due to the fast recombination of charge carriers. In the meantime, photo corrosion poses a threat to bare CdS nanorod arrays in intimate contact with the electrolyte. It is known from our previous work that the highest occupied molecular orbital (LUMO) of PDA is higher than the conduction band (CB) of CdS, and the lowest unoccupied molecular orbital (HOMO) is higher than CdS's valence band (VB) [10, 29, 30]. Thus, whereas the holes tend to converge at the PDA's HOMO energy level, matching bandgap configurations are advantageous for the tandem transfer of photogenerated electrons from PDA to CdS. Meanwhile, the PDA shield obstructs various dissolved free radicals' path of assault, resulting in delayed photo corrosion, this echoes the outcomes and discussions about PEC performance, M-S, and EIS test by comparing the pristine CdS and CdS/PDA. The marriage coupling interfaces of the PDA/FeOOH offer a steady driving force for charge separation with the FeOOH boost. This leads to a decreased charge recombination rate, as the I-t curves, M-S, and EIS data demonstrate. The integration of PDA and FeOOH produces improved PEC water oxidation performance by inducing a synergistic modifying effect for the unstable CdS photoanode and low carrier usage. In summary, we have compiled the various impacts of PDA, as

detailed in Table 1. Only this work has investigated the pass-through capability of photogenerated holes. This significant leap forward fuels optimism in the realm of PEC conversion, positioning the versatile PDA at the epicenter of a novel trajectory for energy conversion technologies.

## 4 Conclusions

The significance of this work lies in exploring the potential of PDA in photoelectric energy conversion. To accomplish this, a dopamine coating that has self-polymerized is used to directly anchor photogenerated hole extractors FeOOH on the surface of a CdS photoanode. The effects of the PDA layer on promoting the photocatalytic performance mainly embody carrier separation and surface passivation for sluggish and photochemical instable CdS. With the boost of FeOOH, the photocurrent density generated by the composite photoelectrode is 1.9 mA $cm^{-2}$, which is 3.39 times greater than the pure CdS photoanode and 1.98 times greater than the CdS/PDA composite photoanode. Ultrathin PDA layer permits photogenerated hole passage was proved from experimental data and legitimate inference. By doing so, it showcases the capacity of PDA to facilitate the passage of photogenerated holes. This effort provides a valuable strategy for the design and assembly of heterogeneous structures by PDA viscous platform, and it is expected to broaden the application of PDA in various photocatalytic reactions involving holes. The present approach highlights the concept of integrating biologically functional layers to stabilize photochemically unstable semiconductors for practical PEC applications.

### Acknowledgments

Zhiru Zhao and Mingyue Wang made equal contributions to this work. The authors acknowledge the financial support from the Liaoning Province Department of Education Fund (6006022016), and the Natural Science Foundation of Jiangxi Province, China (Grant No. 20212BAB204045).

### Conflicts of interest

The authors state that they have no known competing financial interests or personal relationships that could have influenced the work presented in this study.

### References

1 Zhou Z., Qiao H.W., Hou Y., Yang H.G., Yang S. (2021) Epitaxial halide perovskite-based materials for photoelectric energy conversion, *Energy Environ. Sci.* **14**, 1, 127–157.
2 Wang Y., Guo H., Luo X., Liu X., Hu Z., Han L., Zhang Z. (2019) Nonsiliceous mesoporous materials: design and applications in energy conversion and storage, *Small* **15**, 32, 1805277.
3 Jiang Y., Xie H., Han L., Zhang Y., Ding Y., Shen S., Chen B., Ni M. (2023) Advances in $TiS_2$ for energy storage, electronic devices, and catalysis: a review, *Prog. Nat. Sci.* **33**, 2, 133–150.
4 Jiang C., Moniz S.J.A., Wang A., Zhang T., Tang J. (2017) Photoelectrochemical devices for solar water splitting–materialand challenges, *Chem. Soc. Rev.* **46**, 15, 4645–4660.
5 Li Z., Luo L., Li M., Chen W., Liu Y., Yang J., Xu S.-M., Zhou H., Ma L., Xu M., Kong X., Duan H. (2021) Photoelectrocatalytic C-H halogenation over an oxygen vacancy-rich $TiO_2$ photoanode, *Nat. Commun.* **12**, 1, 6698.
6 Gao B., Sun M., Ding W., Ding Z., Liu W. (2021) Decoration of γ-graphyne on $TiO_2$ nanotube arrays: improved photoelectrochemical and photoelectrocatalytic properties, *Appl. Catal. B-Environ.* **281**, 119492.
7 Liu Y., Wygant B.R., Kawashima K., Mabayoje O., Hong T. E., Lee S.E., Lin J., Kim J.H., Yubuta K., Li W., Li J., Mullins C.B. (2019) Facet effect on the photoelectrochemical performance of a $WO_3/BiVO_4$ heterojunction photoanode, *Appl. Catal. B-Environ.* **245**, 227–239.
8 Sivula K., Formal F.L., Grätzel M. (2009) $WO_3$–$Fe_2O_3$ photoanodes for water splitting: a host scaffold, guest absorber approach, *Chem. Mater.* **21**, 13, 2862–2867.
9 Li X., Kan M., Wang T., Qin Z., Zhang T., Qian X., Kuwahara Y., Mori K., Yamashita H., Zhao Y. (2021) The ClO generation and chlorate suppression in photoelectrochemical reactive chlorine species systems on $BiVO_4$ photoanodes, *Appl. Catal. B-Environ.* **296**, 120387.
10 Zheng S., Han L., Luo X., Sun L., Li N., Zhang Z., Li X. (2022) Polydopamine and nafion bi-layer passivation modified CdS photoanode for photoelectrochemical hydrogen evolution, *Int. J. Energy Res.* **46**, 4, 4506–4515.
11 Song J., Su H.Y., Fang M., Han L., Chu J., Li C., Miao R., Yao W., Zhang G., You A. (2022) Photochemical construction of the ZnCdS/PO/FeCoNiPi–MnO composite for efficient tandem application of photocatalytic partial water splitting and overall water splitting, *J. Mater. Chem. A* **10**, 30, 16029–16036.
12 Peng S., Jiang Y., Wang Z., Luo X., Lu J., Han L., Ding Y. (2020) Introducing a porous container and a defect-rich cocatalyst coating over CdS nanoparticles for promotion of photocatalytic hydrogen evolution, *Catal. Lett.* **150**, 12, 3533–3541.
13 Zheng S., Peng S., Wang Z., Huang J., Luo X., Han L., Li X. (2021) Schottky-structured 0D/2D composites via electrostatic self-assembly for efficient photocatalytic hydrogen evolution, *Ceram. Int.* **47**, 20, 28304–28311.
14 Chen S., Huang D., Xu P., Xue W., Lei L., Cheng M., Wang R., Liu X., Deng R. (2020) Semiconductor-based photocatalysts for photocatalytic and photoelectrochemical water splitting: will we stop with photocorrosion? *J. Mater. Chem. A* **8**, 5, 2286–2322.
15 Shen S., Li X., Zhou Y., Han L., Xie Y., Deng F., Huang J., Chen Z., Feng Z., Xu J., Dong F. (2023) Novel $BiOBr/Bi_2S_3$ high-low junction prepared by molten salt method for boosting photocatalytic degradation and $H_2O_2$ production, *J. Mater. Sci. Technol.* **155**, 148–159.
16 Zan Z., Li X., Gao X., Huang J., Luo Y., Han L. (2022) 0D/2D carbon nitride quantum dots (CNQDs)/BiOBr S-scheme heterojunction for robust photocatalytic degradation and $H_2O_2$ production, *Acta Phys. Chim. Sin.* **39**, 6, 2209016.
17 Tang M., Li X., Deng F., Han L., Xie Y., Huang J., Chen Z., Feng Z., Zhou Y. (2023) $BiPO_4$/Ov-BiOBr high-low junctions for efficient visible light photocatalytic performance for tetracycline degradation and $H_2O_2$ production, *Catalysts* **13**, 3, 634.

18 Wang W., Li X., Deng F., Liu J., Gao X., Huang J., Xu J., Feng Z., Chen Z., Han L. (2022) Novel organic/inorganic PDI-Urea/BiOBr S-scheme heterojunction for improved photocatalytic antibiotic degradation and $H_2O_2$ production, *Chin. Chem. Lett.* **33**, 12, 5200–5207.

19 Ge G., Liu M., Liu C., Zhou W., Wang D., Liu L., Ye J. (2019) Ultrathin FeOOH nanosheets as an efficient cocatalyst for photocatalytic water oxidation, *J. Mater. Chem. A* **7**, 15, 9222–9229.

20 Wang T., Long X., Wei S., Wang P., Wang C., Jin J., Hu G. (2020) Boosting hole transfer in the fluorine-doped hematite photoanode by depositing ultrathin amorphous FeOOH/CoOOH cocatalysts, *ACS Appl. Mater. Interfaces* **12**, 44, 49705–49712.

21 Li J., Li F., Jin J. (2021) Hole extraction and injection pathways constructed by the in situ growth of ultra-thin Fe-doped NiOOH Co-catalysts on a fluorine-doped α-$Fe_2O_3$ photoanode, *J. Power Sources* **482**, 228957.

22 Ning X., Li J., Yang B., Zhen W., Li Z., Tian B., Lu G. (2017) Inhibition of photocorrosion of CdS via assembling with thin film $TiO_2$ and removing formed oxygen by artificial gill for visible light overall water splitting, *Appl. Catal. B-Environ.* **212**, 129–139.

23 Ning X., Zhen W., Wu Y., Lu G. (2018) Inhibition of CdS photocorrosion by $Al_2O_3$ shell for highly stable photocatalytic overall water splitting under visible light irradiation, *Appl. Catal. B-Environ.* **226**, 373–383.

24 Wang C., Wang L., Jin J., Liu J., Li Y., Wu M., Chen L., Wang B., Yang X., Su B.L. (2016) Probing effective photocorrosion inhibition and highly improved photocatalytic hydrogen production on monodisperse PANI@CdS core-shell nanospheres, *Appl. Catal. B-Environ.* **188**, 351–359.

25 Farokhi M., Mottaghitalab F., Saeb M.R., Thomas S. (2019) Functionalized theranostic nanocarriers with bio-inspired polydopamine for tumor imaging and chemo-photothermal therapy, *J. Control. Release* **309**, 203–219.

26 Kim Y., Coy E., Kim H., Mrówczyński R., Torruella P., Jeong D.W., Choi K.S., Jang J.H., Song M.Y., Jang D.J., Peiro F., Jurga S., Kim H.J. (2021) Efficient photocatalytic production of hydrogen by exploiting the polydopamine-semiconductor interface, *Appl. Catal. B-Environ.* **280**, 119423.

27 Zhang B., Wang H., Xi J., Zhao F., Zeng B. (2020) In situ formation of inorganic/organic heterojunction photocatalyst of $WO_3$/Au/polydopamine for immunoassay of human epididymal protein 4, *Electrochim. Acta* **331**, 135350.

28 Guo Z., Wang G., Fu H., Wang P., Liao J., Wang A. (2020) Photocatalytic degradation of methylene blue by a cocatalytic PDA/$TiO_2$ electrode produced by photoelectric polymerization, *RSC Adv.* **10**, 44, 26133–26141.

29 Li N., Han L., Zhang H., Huang J., Luo X., Li X., Wang Y., Qian W., Yang Y. (2022) Polydopamine nanolayer assisted internal photo-deposition of CdS nanocrystals for stable cosensitized photoanode, *Nano Res.* **15**, 10, 1–10.

30 Sun L., Han L., Li N., Wang P., Wang M., Luo X., Li X. (2022) P25-induced polydopamine conformal assembly on $Cu_2O$ polyhedra for hydrophilic and stable photoelectrochemical performance, *J. Mater. Chem. C* **10**, 38, 14194–14201.

31 Li N., Zhang Q., Han L., Huang J., Luo X., Li X. (2023) Recent advances in polydopamine and its derivatives assisted electrocatalysis and photocatalysis, *Int. J. Hydrogen Energy* **48**, 19, 7004–7018.

32 Ruan M., Guo D., Jia Q. (2021) A uniformly decorated and photostable polydopamine–organic semiconductor to boost the photoelectrochemical water splitting performance of CdS photoanodes, *Dalton Trans.* **50**, 5, 1913–1922.

33 Yue J., Jiang X., Yu A. (2011) Experimental and theoretical study on the β-FeOOH nanorods: growth and conversion, *J. Nanopart. Res.* **13**, 3961–3974.

34 Dreyer D.R., Miller D.J., Freeman B.H., Paul D.R., Bielawski C.W. (2012) Elucidating the structure of poly (dopamine), *Langmuir* **28**, 15, 6428–6435.

35 Wang H., Wei L., Wang Z., Chen S. (2016) Preparation, characterization and long-term antibacterial activity of Ag-poly(dopamine)-$TiO_2$ nanotube composites, *RSC Adv.* **6**, 17, 14097–14104.

36 Ristić M., Musić S., Godec M. (2006) Properties of γ-FeOOH, α-FeOOH and α-$Fe_2O_3$ particles precipitated by hydrolysis of $Fe^{3+}$ ions in perchlorate containing aqueous solutions, *J. Alloys Compd.* **417**, 1, 292–299.

37 Guo F., Chen J., Zhao J., Chen Z., Xia D., Zhan Z., Wang Q. (2020) Z-scheme heterojunction g-$C_3N_4$@PDA/BiOBr with biomimetic polydopamine as electron transfer mediators for enhanced visible-light driven degradation of sulfamethoxazole, *Chem. Eng. J.* **386**, 124014.

38 Chen F., Yu W., Qie Y., Zhao L., Zhang H., Guo L.H. (2019) Enhanced photocatalytic removal of hexavalent chromium through localized electrons in polydopamine-modified $TiO_2$ under visible irradiation, *Chem. Eng. J.* **373**, 58–67.

39 Perini J.A.L., Torquato L.D.M., Irikura K., Zanoni M.V.B. (2019) Ag/polydopamine-modified Ti/$TiO_2$ nanotube arrays: a platform for enhanced $CO_2$ photoelectroreduction to methanol, *J. $CO_2$ Util.* **34**, 596–605.

40 Li M., Zhang S., Li L., Han J., Zhu X., Ge Q., Wang H. (2020) Construction of highly active and selective polydopamine modified hollow ZnO/$Co_3O_4$ p-n heterojunction catalyst for photocatalytic $CO_2$ reduction, *ACS Sustain. Chem. Eng.* **8**, 11465–11476.

41 Jie X., Bao N., Gong B., Zhou S. (2017) Facile synthesis of plasmonic Ag/AgCl/polydopamine-$TiO_2$ fibers for efficient visible photocatalysis, *Nano-Struct.* **12**, 98–105.